Materialia 24 (2022) 101461

Contents lists available at ScienceDirect

Materialia

journal homepage: www.elsevier.com/locate/mtla

New structure and insight on the phase transition within the Cu-Pd-Sn system with 25 at. % Sn

Monika Amundsen[a], Nicholas A. Pike[a], Ole Martin Løvvik[a,b], Patricia Almeida Carvalho[b], Anette Eleonora Gunnæs[a,*]

[a] Department of Physics, Centre for Materials Science and Nanotechnology, University of Oslo, P. O. Box 1048 Blindern, NO, Oslo 0316, Norway
[b] SINTEF Materials Physics, NO, Oslo 0314, Norway

ARTICLE INFO

Keywords:
Phase transformation
Copper palladium tin
Shape memory alloy
Structure
Martensitic transformation

ABSTRACT

The Cu-Pd-Sn material system has a $(Cu, Pd)_3Sn$ phase region that shows an interesting and unexplored martensitic phase transformation. Literature on this system is limited and the description of the phases present is incomplete and partly contradictory. With focus on a specific Cu-rich composition in this phase region ($Cu_{33}Pd_{42}Sn_{25}$) and having employed a combination of differential scanning calorimetry, X-ray diffraction, optical microscopy and density functional theory (DFT) methods we analyze the phases involved and the phase transformation temperatures. The martensitic transformation was found to occur at approximately 378 K upon heating and at 328 K under cooling conditions. The crystal structure of the high temperature (HT) austenite phase was identified as face centered cubic with lattice constant $a = 6.2261(1)$ Å at 473 K. DFT simulations of plausible atomic arrangements indicated that the HT phase was an $L2_1$ ($Fm\bar{3}m$) type structure. The martensitic LT phase was found to be orthorhombic with a $D0_{11}$ ($Pnma$) type structure with lattice parameters $a = 8.9860(3)$ Å, $b = 5.9347(2)$ Å and $c = 4.5328(2)$ Å at 298 K.

1. Introduction

The search for new and better shape memory alloys (SMAs) has been of increasing interest in the scientific community as potential applications for these materials are expanding [1]. SMAs are the basis of devices spanning from novel solid-state actuators [2], medical implants [3], caloric [4,5] to energy harvesting applications [6–8], and morphing aerostructures have recently been proposed for structural applications [9].

SMAs undergo a highly reversible, diffusionless solid-to-solid martensitic phase transformation from a high symmetry, high temperature (HT) austenite phase to a low symmetry, low temperature (LT) martensite phase [10]. The transformation is temperature-driven in the case of the shape memory effect and stress-driven in the case of superelasticity. Along with the structural change, a change in another property, such as a mechanical [11] or electromagnetic [8,12] property, might follow, making SMAs attractive in a range of applications [1].

A major limiting factor for large-scale implementation of SMAs is structural and functional fatigue, especially for high-cycle applications [13]. It is commonly believed that the stress transition layer, originating from poor compatibility between the austenite and martensite phases, is the main contributor to the degradation of SMAs [14,15]. This transition layer gives rise to an energy barrier that causes hysteresis [16] and leads to the eventual failure of the material.

Theoretical conditions of compatibility have been presented in the literature [14,16,17]. These conditions are evaluated based on a transformation stretch matrix, which is constructed using knowledge of the lattice parameters and the space group of the martensite and austenite phases [18]. These theories state that when the middle eigenvalue of the transformation stretch matrix equals unity ($\lambda_2 = 1$) perfect compatibility between a single variant of unstressed martensite and austenite may be obtained [14,16]. Recently, even stronger conditions of compatibility have been put forward through the so-called *cofactor conditions* [17]. The cofactor conditions predict the possibility of several unstressed interfaces, thus giving *supercompatibility* between the phases [17,19]. Materials that closely satisfy the cofactor conditions have been shown to display small hysteresis and a high level of reversibility [20,21]. This has led to the discovery of materials with outstanding fatigue properties, such as $Au_{30}Cu_{25}Zn_{45}$ [22] and $Ti_{54}Ni_{34}Cu_{12}$ [21] displaying reversible transitions without significant degradation up to 10^5 and 10^7 cycles, respectively.

Cu-Pd-Sn alloys with 25 at. % Sn show a martensitic phase transformation [23]. With the high solubility of Cu on the Pd site, lattice parameters, and hence the cofactors conditions, can potentially be tuned to tailor materials with improved compatibility and thus improved fa-

* Corresponding author.
E-mail address: a.e.gunnas@fys.uio.no (A.E. Gunnæs).

https://doi.org/10.1016/j.mtla.2022.101461
Received 8 November 2021; Accepted 21 May 2022
Available online 25 May 2022

tigue properties [24]. So far, only a limited number of reports exist on the Cu-Pd-Sn system [23,25–32] and fundamental studies are needed for further understanding of their phase transforming properties.

The earliest found studies on ternary Cu-Pd-Sn were performed by Evstigneeva and Nekrasov who reported on phases and phase relations in the pseudobinary Pd_3Sn-Cu_3Sn phase diagram up to 30 at. % Cu [25]. The phase region was further described in a paper by Evstigneeva and Genkin [23] where a phase transition was reported to take place at 473 K in a sample of composition $Cu_{25}Pd_{50}Sn_{25}$. The HT phase was identified as cubic with lattice parameter a = 3.89 Å at 487 K and was described as a solid solution of Cu on the Pd sites $(Cu, Pd)_3Sn$, hence isostructural to cubic Pd_3Sn. The LT phase was identified as orthorhombic with $a = b$ = 7.88(5) Å and c = 3.94(2) Å and can be compared with its mineral equivalent Cabriite, which has been presented in detail by Wilson et al. [26]. Structure determination of the low-temperature phase was not possible due to finely twinned aggregate grains, thus the space groups were not determined.

More recently, isothermal sections of the Cu-Pd-Sn system at 773 and 1073 K have been described by Kareva et al. [31]. The data was based on numerous specimens annealed at 773 and 1073 K, quenched, and characterized at room temperature. In contrast to the reports by Evstigneeva and Genkin, Pd-rich $(Cu, Pd)_3Sn$ samples were described with an orthorhombic structure at both 773 and 1073 K. The $(Cu, Pd)_3Sn$ phase region was reported to stretch from 9 to 32 at. % Cu at 773 K and from 12 to 35 at. % Cu at 1073 K, both with 25 at. % Sn.

Kareva et al. also reported a fine twin-intergrowth structure making it unachievable to obtain single crystals to clarify atomic positions and, due to similar X-ray scattering factors for Pd and Sn, the structure type was not identified. However, the space group was determined as *Pnma* (#62) for the composition $Cu_{25}Pd_{50}Sn_{25}$, with lattice parameters a = 8.980(3) Å, b = 5.9234(16) Å and c = 4.5311(2) Å.

The present paper aims to give new insight into the previously reported phase transformation and the two transforming phases. By combining theoretical and experimental tools we have determined the transformation temperature and the full crystal structure of the two phases involved.

2. Methodology

In the present study, a sample with composition $Cu_{33}Pd_{42}Sn_{25}$ was prepared by flame melting high purity Cu, Pd and Sn metal powders in a sealed and evacuated quartz ampule. The sample was homogenized at 1123 K for one week and subsequently quenched in water before a second heat treatment at 623 K for 60 h. Powder samples were prepared by crushing and, to remove any internal strain introduced by the crushing process, the powders were annealed in sealed and evacuated quartz ampules using zirconium as getter. The samples were annealed for three hours at 573 K in a tubular resistance heating furnace and subsequently quenched in water.

The microstructure was investigated by optical microscopy using a Reichert-Jung MeF3 instrument with cross-polarized light. The sample temperature was adjusted qualitatively using a heat gun.

A Bruker D8-A25 diffractometer with a Ge (111) Johanssen monochromator and a Lynxeye detector for high-resolution X-ray powder diffraction (XRD) was used to characterize the crystal structure of the powder sample. The diffractometer utilized Cu $K_{\alpha 1}$ radiation and transmission capillary geometry. The sample was quenched to 123 K, then scanned in the 2θ range from 20° to 90° at 298 K. Temperature-dependent properties were investigated in the 2θ range 39° to 45° and with heating steps of 2°, using an Oxford instruments cryodrive attachment. The obtained diffractograms were analyzed using the proprietary TOPAS V5 software.

Phase transformation temperatures were identified by differential scanning calorimetry (DSC) using a Perkin Elmer (DSC 8500) instrument. The sample (19.8 mg of powder in standard pan N5390123) was investigated between 148 K and 488 K, using heating and cooling rates of 10 K/min and with nitrogen as a protecting gas. The transformation temperatures were determined using the tangent method where A_s and A_f correspond to the austenite start and finish temperatures and M_s and M_f correspond to the martensite start and finish temperatures, respectively [33].

Theoretical calculations utilizing first-principles density functional theory (DFT) within the Vienna ab-initio simulation package (VASP) [34–36] were used to complement the experimentally obtained results. Within VASP, our calculations used the projector-augmented wave (PAW) method [37], describing core electrons using PAW pseudopotentials [38] and exchange and correlations effects with the Perdew-Burke-Ernzerhof (PBE) generalized gradient approximation (GGA) [39]. To describe the electronic system, a plane-wave energy cutoff of 500 eV was used and a Monkhorst-Pack [40] mesh of points was generated assuming a k-point density of at least five points per $Å^{-1}$. All structures were relaxed allowing for simultaneous changes to the atomic positions and the unit cell lattice parameters. The relaxation criterion required that the remaining forces be less than 0.01 eV/Å. For each ground-state calculation, the iterations of the total energy were stopped once the differences in energy between successive iterations were less than 0.01 meV per unit cell. Some of the compounds studied exhibit solid solutions of atomic species on one of the sublattices. These structures were represented by special quasi-random structures (SQS), which are designed to mimic the radial correlation functions of a perfectly random structure [41]. Structures containing 104 atoms were generated with a Monte-Carlo algorithm as implemented in the temperature-dependent effective potential (TDEP) package [42]. They were relaxed to their ground-state cubic crystal structures by successive ionic and volume relaxations (in total five relaxations), avoiding VASP's symmetry-breaking relaxation of the supercell lattice parameters. The formation enthalpy H_{form} was defined as the enthalpy difference between these supercells and the corresponding number of metal atoms in their standard state. This enthalpy corresponds to the total electronic energy calculated by DFT and is based on the assumption that contributions from volume change of the bulk materials are negligible compared to the internal energy.

3. Results and discussion

3.1. Phase transformation

In agreement with previous reports [23,31], a twinned microstructure was observed after quenching the sample from elevated temperatures. The twinned regions were found to be optically active when imaged with cross-polarized light as depicted in Fig. 1 (a). Upon heating, the twinning features disappeared abruptly and the sample became optically inactive as depicted in Fig. 1 (b). This change in optical properties is consistent with a martensitic phase transformation from a non-cubic to a cubic structure.

The phase transformation temperatures obtained from DSC data are depicted in Fig. 2, where A_s, A_f, M_s and M_f were found to be approximately 378 K, 382 K, 328 K and 323 K, respectively, with hysteresis ($\Delta T_{hys} = (A_s + A_f - M_s - M_f)/2$) of 54.65 K.

The phase transformation was also observed by in situ XRD, as depicted in Fig. 3 (a). Upon heating from room temperature to 403 K a clear change in the intensity profile in the selected 2θ range (39–45°) can be seen. The Bragg reflection at 2θ = 40.9° (marked "A") indicates HT austenite while those at 2θ = 39.9°, 40.1° and 41.5° (marked "M") denote the LT martensite. The phase transformation upon heating starts at around 363 K, which is slightly lower than what was recorded by DSC (378 K). This discrepancy may be related to differences in thermal history and internal strain in the samples, as the phase transformation temperature is known to shift when cycling a sample with poor A/M compatibility [13].

It should be noted that the transition temperature recorded by XRD, as well as with DSC, for the $Cu_{33}Pd_{42}Sn_{25}$ composition are all

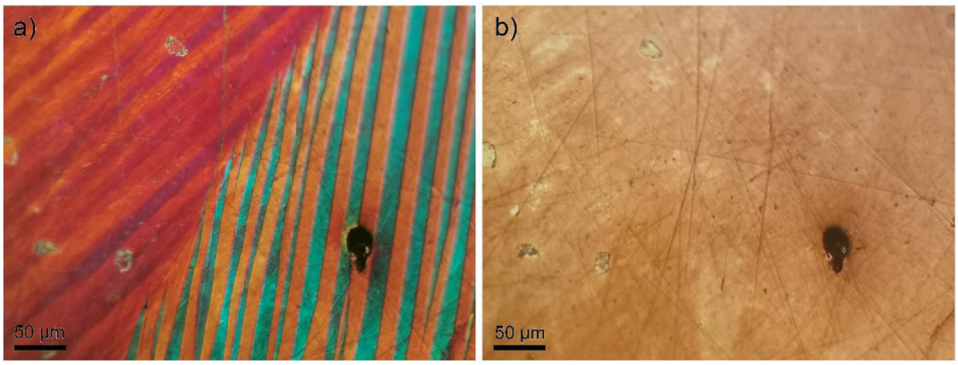

Fig. 1. Polarized optical micrographs of $Cu_{33}Pd_{42}Sn_{25}$ depicted at (a) room temperature with sample in the martensitic phase and (b) at an elevated temperature in the austenitic phase.

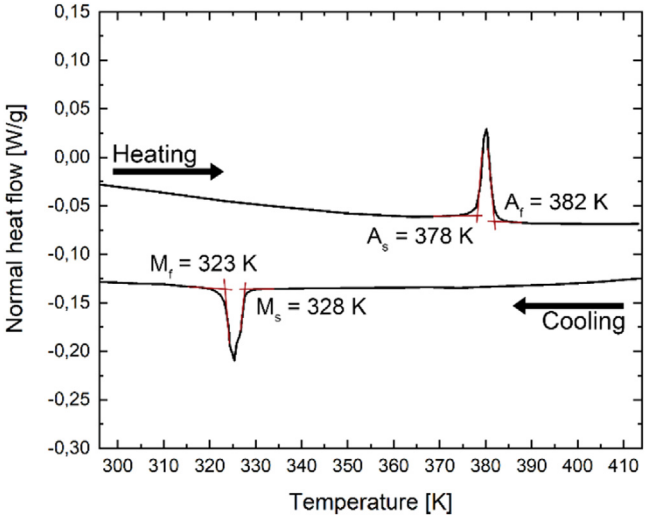

Fig. 2. Differential scanning calorimetry curves of the martensitic transformation, showing the austenite start temperature at approximately 378 K and martensite start temperature at 328 K. The black line corresponds to the experimental trace.

well below 473 K that was previously reported for $Cu_{25}Pd_{50}Sn_{25}$ by Evstigneeva et al. [23]. Hence, this is an indication that the transition temperature is composition-dependent within the $(Cu, Pd)_3Sn$ phase region.

3.2. Austenite structure determination

In order to solve the crystal structure of the phases, XRD was performed on the austenite and martensite phases of $Cu_{33}Pd_{42}Sn_{25}$. The resulting diffractograms are depicted in Fig. 3 (b) and (c).

The characteristic Bragg peaks of the HT phase, marked by circles in Fig. 3 (b), imply a face-centered cubic (FCC) unit cell with lattice parameter $a = 6.226$ Å. This is inconsistent with the previously reported primitive cubic HT phase, with space group $Pm\bar{3}m$ (#221) and $a = 3.89$ Å [23], thus revealing a new unreported cubic HT phase in the $(Cu, Pd)_3Sn$ system. While it was straightforward to identify the Bravais unit cell, deducing the atomic positions from the XRD intensities is more challenging due to the similar X-ray scattering factors of Pd and Sn.

However, the number of plausible structure types of the cubic HT phase is limited. From the size and symmetry of the unit cell, 16 atoms can be expected in the conventional FCC unit cell. For the $CuPd_2Sn$ phase there are three likely structure types: $AlCu_2Mn$ (full Heusler, $L2_1$ ($Fm\bar{3}m$, #225)), BiF_3 ($D0_3$, ($Fm\bar{3}m$, # 225)) and $AgLi_2Sb$ (inverse Heusler, XA ($F\bar{4}3m$, #216)) as illustrated in Fig. 4. In the stoichiometric ($Cu_{25}Pd_{50}Sn_{25}$) $L2_1$ structure, Sn (red balls) occupies the 4*a* positions, while Cu (blue balls) and Pd (yellow balls) occupy the 4*b* and 8*c* positions, respectively. In the non-stoichiometric $Cu_{33}Pd_{42}Sn_{25}$ composition, some of the 8*c* positions will be occupied by Cu as illustrated with two-colored balls. In the $D0_3$ structure, Sn occupies the 4a positions, while Cu and Pd are disordered on the 4*b* and 8*c* sites. Like in the $L2_1$-Heusler structure, the atoms in the stoichiometric XA inverse Heusler structure are ordered: Pd on 4*a* and 4*c*, Cu on 4*d* and Sn on 4*b* sites, while for the non-stoichiometric $Cu_{33}Pd_{42}Sn_{25}$, some of the 4*a*/4*c* positions will be occupied by Cu.

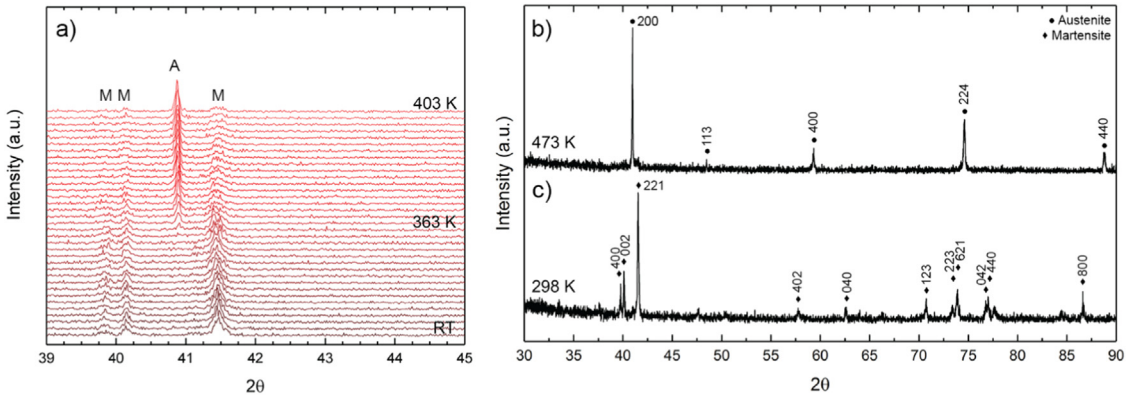

Fig. 3. X-ray powder diffractograms of $Cu_{33}Pd_{42}Sn_{25}$ were recorded with increasing temperature from room temperature to 403 K (a) where a phase transformation from the martensite (M) to austenite (A) is found to start around 363 K. In (b) and (c) diffractograms were recorded at constant temperature (473 K (b) and 298 K (c)) where circles and diamonds mark Bragg peaks indexed according to a cubic $L2_1$ phase and an orthorhombic $D0_{11}$ phase, respectively.

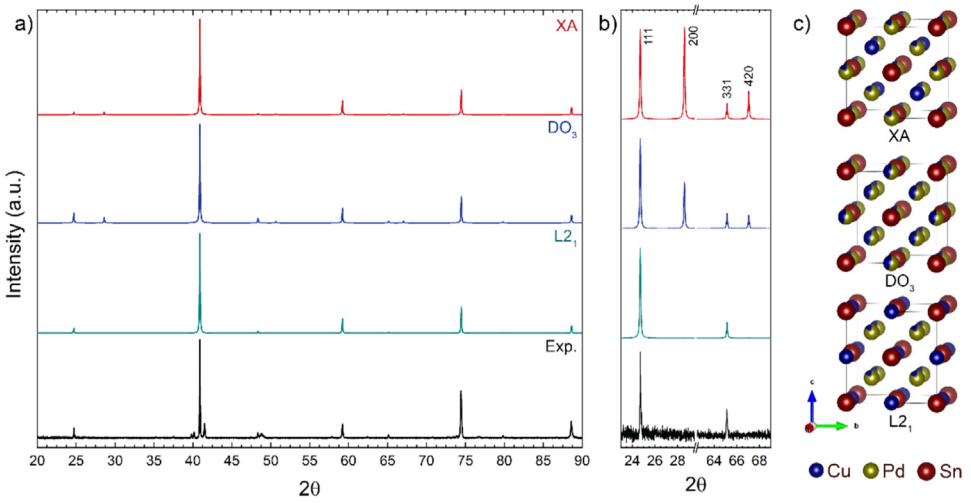

Fig. 4. Comparison of simulated diffractograms of structure candidates for the HT FCC phase: XA, $D0_3$ and $L2_1$, to the experimental data, with (a) overall view and (b) detailed selection. (c) Depicted structural models of the possible symmetries. Visualization of structural models and theoretical XRD power spectra by [43].

Diffractograms of the three candidate structures were simulated and compared to the experimental diffractogram as presented in Fig. 4 (a). This reveals prominent differences in the intensity of the weak reflections (111), (200), (311) and (420), as highlighted in the zoomed-in regions in Fig. 4 (b). Most notably, the absence of the (200) and (420) reflection in the experimental data is a strong indication that $L2_1$ is the appropriate HT structure.

DFT calculations were performed to corroborate the experimental findings and quantify the relative stability of the three cubic structure candidates $D0_3$, $L2_1$ and XA described above. The simulations were performed at the composition used in the present paper ($Cu_{33}Pd_{42}Sn_{25}$) and at the $Cu_{25}Pd_{50}Sn_{25}$ composition used in previous papers [23,31]. Predicted electronic enthalpies are presented in Table 2 and relaxed crystal structures in Fig. 4 (c).

The theoretical calculations suggest that the most stable cubic structure candidate (i.e., the structure among $D0_3$, XA, and $L2_1$ with the most negative formation enthalpy) for both $Cu_{25}Pd_{50}Sn_{25}$ and $Cu_{33}Pd_{42}Sn_{25}$ is $L2_1$. The enthalpy differences between the structures are not large, but significant within the level of theory (ground state ($T = 0$ K) DFT at the GGA level). The present precision parameters warrant a numerical uncertainty of less than 0.02 kJ/mole of atoms. Five different SQS models were used for each composition to obtain a representative selection of structural motifs, and the enthalpy of formation varied by less than 0.07 kJ/mole of atoms between the different models. The results are thus robust and reproducible. This is supported by the comparison between the calculated and experimentally measured formation enthalpy of the LT $D0_{11}$ phase, which is reasonable given the differing composition (Table 2).

The observed phase transformation in the present study is martensitic, and a close relationship between the unit cells of the HT and the LT phase should exist. The lattice parameters of the LT phase can be described as: $a_{LT} = \sqrt{2}\, a_{HT}$, $b_{LT} = a_{HT}$ and $c_{LT} = a_{HT}/\sqrt{2}$.

3.3. Martensite structure determination

The diffractogram of the LT phase, obtained at 298 K, is presented in Fig. 3 (b). The characteristic Bragg peaks of the LT phase, marked with diamonds, were indexed in agreement with an orthorhombic unit cell with space group *Pnma* and lattice parameters as listed in Table 1. This is similar to the reported structure of the related compound $Cu_{25}Pd_{50}Sn_{25}$ reported by [31], also listed in Table 1. The volumes of the unit cells differ by less than 0.1% despite the difference in composition.

The orthorhombic structure in [31] was interpreted as a HT phase since the investigated samples were quenched from high temperatures.

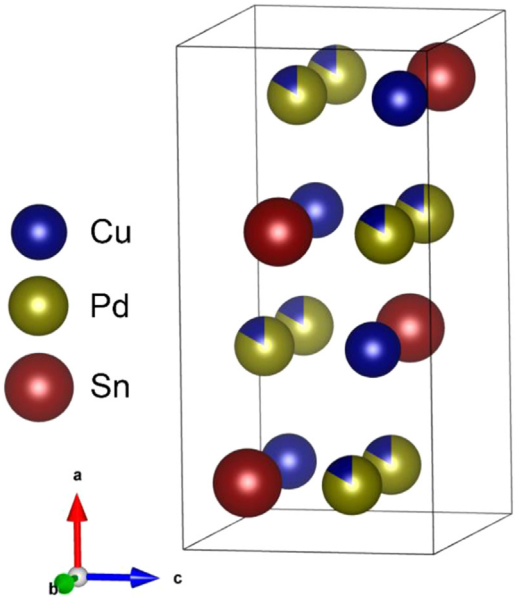

Fig. 5. Structure model of $D0_{11}$ (Pnma) LT phase. Visualization of structural models by [43].

However, with the insight from the present study, it is clear that they correspond to the orthorhombic LT structure. This is also consistent with the phase transformation between an LT orthorhombic and a HT cubic phase reported in Ref. [23]. The unit cell of the LT phase was not identified, but the space group *Pmmm* (#47) was suggested.

The present study concluded that the LT crystal structure is orthorhombic in the *Pmmm* space group in agreement with [31]. However, efforts to reliably refine the atomic positions failed due to finely twinned crystallographic grains and similar scattering factors of Pd and Sn, similar to what was experienced by [23] and [31]. DFT calculations were instead used to relax the atomic positions in both $Cu_{25}Pd_{50}Sn_{25}$ and $Cu_{33}Pd_{42}Sn_{25}$, presented in Table 3, suggesting that the LT phase corresponds to a $D0_{11}$ atomic arrangement as illustrated in Fig. 5.

To investigate the possible reversibility of the $Cu_{33}Pd_{42}Sn_{25}$ sample, the transformation stretch matrix was determined as shown in Ref. [18]. Lattice parameters used for the calculations were obtained by XRD as presented in Table 1. The calculated transformation matrix between the

Table 1
Lattice parameters obtained from X-ray diffraction data and DFT calculations. The DFT results are taken from the most stable structures identified in.

	HT ($Fm\bar{3}m$)	LT (Pnma)			
Composition	a (Å)	a (Å)	b (Å)	c (Å)	
$Cu_{33}Pd_{42}Sn_{25}$	6.2261(1)	8.9860(3)	5.9347(2)	4.5328(2)	Current work, HT 473 K, LT 298 K (XRD)
$Cu_{33}Pd_{42}Sn_{25}$	6.2238(1)	8.956(6)	5.963(4)	4.507(4)	Current work, At transition 343K (XRD)
$Cu_{33}Pd_{42}Sn_{25}$	6.309	9.160	5.925	4.630	Current work, 0 K (DFT)
$Cu_{25}Pd_{50}Sn_{25}$	6.334	9.243	5.628	4.706	Current work, 0 K (DFT)
$Cu_{25}Pd_{50}Sn_{25}$		8.980(3)	5.9234(16)	4.5311(2)	[31], RT (XRD)
$Cu_{25}Pd_{50}Sn_{25}$	3.89*	7.88(5)*	7.88(5)*	3.94(2)*	[23], LT 466 K, HT 487 K (XRD)

* Space groups were not determined but $Pm\bar{3}m$ and Pmma were suggested.

Table 2
Formation enthalpy in kJ/mole of atoms for the three HT cubic crystal structure candidates $D0_3$, XA, and $L2_1$ of $Cu_{33}Pd_{42}Sn_{25}$ and $Cu_{25}Pd_{50}Sn_{25}$, compared to that of the LT $D0_{11}$ (*Pnma*) phase.

Composition	$D0_3$	XA	$L2_1$	$D0_{11}$	Expt.
$Cu_{33}Pd_{42}Sn_{25}$	-26.9	-25.6	-30.1	-28.4	
$Cu_{25}Pd_{50}Sn_{25}$	-33.4	-27.6	-38.3	-40.5	-43.1[a]

[a] Composition $Cu_{20.5}Pd_{56.0}Sn_{23.5}$ [44]

Table 3
Suggested atom position from DFT calculations for the $D0_{11}$ (Pnma) LT phase.

Site	Wyckoff position	x	y	z	Atom	Occ.
$Cu_{25}Pd_{50}Sn_{25}$						
Pd	8d	0.135	0.000	0.678	Pd	1
Cu	4c	0.386	0.250	0.682	Cu	1
Sn	4c	0.116	0.250	0.190	Sn	1
$Cu_{33}Pd_{42}Sn_{25}$						
Pd	8d	0.138	0.000	0.700	Pd/Cu	0.84/0.16
Cu	4c	0.383	0.253	0.694	Cu	1
Sn	4c	0.110	0.257	0.206	Sn	1

two phases is

$$U = \begin{bmatrix} 0.958 & 0 & 0 \\ 0 & 1.021 & 0.003 \\ 0 & 0.002 & 1.021 \end{bmatrix}, \quad (1)$$

whose eigenvalues are $\lambda_1 = 0.958, \lambda_2 = 1.018$ and $\lambda_3 = 1.024$. The λ_2 value clearly differs from unity, which can partially explain the relatively large hysteresis seen for this composition. In addition, complex, multilevel twin structures were observed in the $L2_1$ phase, extending over several length scales. This can facilitate a transformation path different from traditional martensitic theory [45,46].

Nevertheless, λ_2 is not too far from unity, and there is solid solubility of Cu on the Pd position within the $(Cu, Pd)_3Sn$ phase. It may therefore be possible to tune the composition, and thus the lattice parameters, to find a composition closely satisfying the cofactor conditions within this system. Ongoing investigations indicate that changing the composition can indeed lead to λ_2 closer to unity and significantly reduced hysteresis.

The calculated electronic enthalpies in Table 2 suggest that the LT phase is more stable than the most stable HT phase in the case of $Cu_{25}Pd_{50}Sn_{25}$, while the cubic HT phase is the most stable in the case of $Cu_{33}Pd_{42}Sn_{25}$. However, these are valid at ground state (0 K) and several significant contributions to the total Gibbs free energy are neglected. Notably, this includes the phonon free energy, the electronic entropy, and the compositional entropy. We expect that the transformation is temperature-driven and that the difference in compositional entropy and phonon free energy is large between the LT and HT phases. A theoretical quantification of this would require extensive phonon-based thermodynamic calculations beyond the scope of this study. Therefore, since no meaningful assessment of their relative stability can be made solely based on the electronic enthalpies, such an assessment has not been performed (Eq. (1)).

4. Summary

In the current study, we have solved the partial contradictions reported on the Cu-Pd-Sn system in the literature. We have observed and analyzed the phases and martensitic phase transformation of $Cu_{33}Pd_{42}Sn_{25}$. The austenite and martensite phases of $Cu_{33}Pd_{42}Sn_{25}$ were characterized using XRD and DSC to determine temperature-dependent lattice parameters and transition temperatures. The following conclusions have been drawn:

1 $Cu_{33}Pd_{42}Sn_{25}$ undergoes a martensitic phase transformation with $A_s = 378K$, $A_f = 382K$, $M_s = 328K$, and $M_f = 323K$.
2 The low-temperature phase of $Cu_{33}Pd_{42}Sn_{25}$ is $D0_{11}$ (*Pnma*) with lattice parameters $a = 8.9860(3)$ Å, $b = 5.9347(2)$ Å, and $c = 4.5328(2)$ Å.
3 The high-temperature phase is $L2_1$ ($Fm\bar{3}m$) with lattice parameter $a = 6.2261(1)$ Å.
4 The middle eigenvalue of the transformation stretch matrix is $\lambda_2 = 1.018$.

Declaration of Competing Interest

The authors declare that they have no known competing financial interests or personal relationships that could have appeared to influence the work reported in this paper.

Acknowledgments

The authors would like to thank Ole Bjørn Karlsen at the University of Oslo for numerous invaluable contributions, Huiting Jin at SINTEF Industry, and David Wragg at UiO for help with the DSC and XRD experiments. This work was supported by the Research Council of Norway through the COMET project [grant number 262776] and UNINETT Sigma2 [grant numbers nn2615k and nn9462k]. The authors declare that they have no known competing financial interests or personal relationships that could have appeared to influence the work reported in this paper.

Bibliography

[1] J. Mohd Jani, M. Leary, A. Subic, M.A. Gibson, A review of shape memory alloy research, applications and opportunities, Mater. Des. 56 (2014) 1078–1113, doi:10.1016/j.matdes.2013.11.084.
[2] M. Kohl, Shape Memory Microactuators, 1st ed., Springer-Verlag Berlin Heidelberg, 2004, doi:10.1007/978-3-662-09875-2.
[3] T. Duerig, A. Pelton, D. Stockel, An overview of nitinol medical applications, Mater. Sci. Eng. 273 (1999) 149–160, doi:10.1016/S0921-5093(99)00294-4.
[4] J. Cui, Y. Wu, J. Muehlbauer, Y. Hwang, R. Radermacher, S. Fackler, M. Wuttig, I. Takeuchi, Demonstration of high efficiency elastocaloric cooling with large ΔT using NiTi wires, Appl. Phys. Lett. (2012) 101, doi:10.1063/1.4746257.

[5] F. Bruederlin, L. Bumke, C. Chluba, H. Ossmer, E. Quandt, M. Kohl, Elastocaloric cooling on the miniature scale: a review on materials and device engineering, Energy Technol. 6 (2018) 1588–1604, doi:10.1002/ente.201800137.

[6] M. Gueltig, H. Ossmer, M. Ohtsuka, H. Miki, K. Tsuchiya, T. Takagi, M. Kohl, High frequency thermal energy harvesting using magnetic shape memory films, Adv. Energy Mater. (2014), doi:10.1002/aenm.201400751.

[7] H. Ossmer, C. Chluba, S. Kauffmann-Weiss, E. Quandt, M. Kohl, TiNi-based films for elastocaloric microcooling - Fatigue life and device performance, APL Mater. 4 (2016), doi:10.1063/1.4948271.

[8] V. Srivastava, Y. Song, K. Bhatti, R.D. James, The direct conversion of heat to electricity using multiferroic alloys, Adv. Energy Mater. 1 (2011) 97–104, doi:10.1002/aenm.201000048.

[9] D.J. Hartl, D.C. Lagoudas, Aerospace applications of shape memory alloys, Proc. Inst. Mech. Eng. Part G J. Aerosp. Eng. 221 (2007) 535–552, doi:10.1243/09544100JAERO211.

[10] C. Lexcellent, Shape-Memory Alloys Handbook, ISTE/Wiley, 2013, doi:10.1002/9781118577776.

[11] C. Bechtold, C. Chluba, R. Lima De Miranda, E. Quandt, High cyclic stability of the elastocaloric effect in sputtered TiNiCu shape memory films, Appl. Phys. Lett. (2012) 101, doi:10.1063/1.4748307.

[12] J. Liu, T. Gottschall, K.P. Skokov, J.D. Moore, O. Gutfleisch, Giant magnetocaloric effect driven by structural transitions, Nat. Mater. 11 (2012) 620–626, doi:10.1038/nmat3334.

[13] R. Zarnetta, R. Takahashi, M.L. Young, A. Savan, Y. Furuya, S. Thienhaus, B. Maaß, M. Rahim, J. Frenzel, H. Brunken, Y.S. Chu, V. Srivastava, R.D. James, I. Takeuchi, G. Eggeler, A. Ludwig, Identification of quaternary shape memory alloys with near-zero thermal hysteresis and unprecedented functional stability, Adv. Funct. Mater. 20 (2010) 1917–1923, doi:10.1002/adfm.200902336.

[14] J.M. Ball, R.D. James, Fine phase mixtures as minimizers of energy, Arch. Ration. Mech. Anal. 100 (1987) 13–52, doi:10.1007/BF00281246.

[15] K. Bhattacharya, S. Conti, G. Zanzotto, J. Zimmer, Crystal symmetry and the reversibility of martensitic transformations, Nature 428 (2004) 55–59, doi:10.1038/nature02378.

[16] Z. Zhang, R.D. James, S. Müller, Energy barriers and hysteresis in martensitic phase transformations, Acta Mater. 57 (2009) 4332–4352, doi:10.1016/j.actamat.2009.05.034.

[17] X. Chen, V. Srivastava, V. Dabade, R.D. James, Study of the cofactor conditions: conditions of supercompatibility between phases, J. Mech. Phys. Solids 61 (2013) 2566–2587, doi:10.1016/j.jmps.2013.08.004.

[18] X. Chen, Y. Song, N. Tamura, R.D. James, Determination of the stretch tensor for structural transformations, J. Mech. Phys. Solids 93 (2016) 34–43, doi:10.1016/j.jmps.2016.02.009.

[19] H. Gu, L. Bumke, C. Chluba, E. Quandt, R.D. James, Phase engineering and supercompatibility of shape memory alloys, Mater. Today 21 (2018) 265–277, doi:10.1016/j.mattod.2017.10.002.

[20] Y. Song, X. Chen, V. Dabade, T.W. Shield, R.D. James, Enhanced reversibility and unusual microstructure of a phase-transforming material, Nature 502 (2013) 85–88, doi:10.1038/nature12532.

[21] C. Chluba, W. Ge, R.L. DeMiranda, J. Strobel, L. Kienle, E. Quandt, M. Wuttig, Ultralow-fatigue shape memory alloy films, Science 348 (2015) 1004–1007, doi:10.1126/science.1261164.

[22] X. Ni, J.R. Greer, K. Bhattacharya, R.D. James, X. Chen, Exceptional resilience of small-scale $Au_{30}Cu_{25}Zn_{45}$ under cyclic stress-induced phase transformation, Nano Lett. 16 (2016) 7621–7625, doi:10.1021/acs.nanolett.6b03555.

[23] T.L. Evstigneeva, A.D. Genkin, Cabriite Pd_2SnCu, a new species in the mineral group of palladium, tin and copper compounds, Can. Mineral. 21 (1983) 481–487.

[24] N.A. Pike, A. Matt, O.M. Løvvik, Determining the optimal phase-change material via high-throughput calculations, MRS Adv. 4 (2019) 2679–2687, doi:10.1557/adv.2019.235.

[25] T.L. Evstigneeva, L.Y. Nekrasov, Conditions of phase synthesis and phase relations in the systems Pd_3Sn-Cu_3Sn and Pd-Sn-Cu-HCl (in Russian), Contrib. Phys. Chem. Petrol 9 (1980) 20–35.

[26] G.C. Wilson, J.C. Rucklidge, C. Cermignani, Coarse-Grained Cabriite from Noril'sk, Russia, Can. Mineral. 40 (2002) 473–479, doi:10.2113/gscanmin.40.2.473.

[27] V. Kuznetsov, L.B. Copper-Palladium-Tin, Numerical Data and Functional Relationships in Science and Technology (New Series). Group IV: Physical Chemistry. Non–Ferrous Metal Systems. Part 3. Selected Soldering and Brazing Systems, Springer, Berlin, 2007.

[28] M.A. Kareva, E.G. Kabanova, G.P. Zhmurko, V.N. Kuznetsov, A.V. Yatsenko, Phases of the NiAs family in Cu-Pd-Sn and Au-Pd-Sn systems, Russ. J. Inorg. Chem. 57 (2012) 502–507, doi:10.1134/S0036023612030114.

[29] M.A. Rahman, C.W. Fan, S.J. Wang, C.E. Ho, W. Gierlotka, Experimental studies and thermodynamic assessment of ternary Cu-Pd-Sn phase relations focusing on the Sn-rich alloys, J. Electron. Mater. 43 (2014) 176–186, doi:10.1007/s11664-013-2735-4.

[30] M. Hashiba, W. Shinmei, M. Kajihara, Kinetics of reactive diffusion in the (Pd-Cu)/Sn system at solid-state temperatures, J. Electron. Mater. 43 (2014) 247–258, doi:10.1007/s11664-013-2722-9.

[31] M.A. Kareva, E.G. Kabanova, K.B. Kalmykov, G.P. Zhmurko, V.N. Kuznetsov, Isothermal sections of Pd-Cu-Sn system at 500 and 800°C, J. Phase Equilibria Diffus. 35 (2014) 413–420, doi:10.1007/s11669-014-0299-5.

[32] M.A. Kareva, E.G. Kabanova, G.P. Zhmurko, E.A. Ptashkina, D.D. Elnyakov, V.N. Kuznetsov, Melting surface of a solid solution based on palladium, gold, and copper with tin additives, Russ. Chem. Bull. 67 (2018) 211–214, doi:10.1007/s11172-018-2061-3.

[33] J.M. Guilemany, F.J. Gil, The Gibbs free energies of thermal and stress-induced martensite formation in Cu-Zn-Al single crystal shape-memory alloys, Thermochim. Acta. 182 (1991) 193–199, doi:10.1016/0040-6031(91)80004-3.

[34] G. Kresse, J. Furthmüller, Efficient iterative schemes for ab initio total-energy calculations using a plane-wave basis set, Phys. Rev. B 54 (1996) 169–186, doi:10.1103/PhysRevB.54.11169.

[35] G. Kresse, J. Furthmüller, Efficiency of ab-initio total energy calculations for metals and semiconductors using a plane-wave basis set, Comput. Mater. Sci. 6 (1996) 15–50, doi:10.1016/0927-0256(96)00008-0.

[36] G. Kresse, J. Hafner, Ab initio molecular dynamics for open-shell transition metals, Phys. Rev. B 48 (1993) 115–118, doi:10.1103/PhysRevB.48.13115.

[37] P.E. Blöchl, Projector augmented-wave method, Phys. Rev. B 50 (1994) 953–979, doi:10.1103/PhysRevB.50.17953.

[38] G. Kresse, D. Joubert, From ultrasoft pseudopotentials to the projector augmented-wave method, Phys. Rev. B 59 (1999) 1758–1775, doi:10.1103/PhysRevB.59.1758.

[39] J.P. Perdew, K. Burke, M. Ernzerhof, Generalized Gradient Approximation Made Simple, Phys. Rev. Lett. 77 (1996) 3865–3868, doi:10.1103/PhysRevLett.77.3865.

[40] H.J. Monkhorst, J.D. Pack, Special points for Brillonin-zone integrations, Phys. Rev. B 13 (1976) 5188–5192, doi:10.1103/PhysRevB.13.5188.

[41] A. Zunger, S.-H. Wei, L.G. Ferreira, J.E. Bernard, Special Quasirandom Structures, Phys. Rev. Lett. 65 (1990) 353–356, doi:10.1103/PhysRevLett.65.353.

[42] O. Hellman, P. Steneteg, I.A. Abrikosov, S.I. Simak, Temperature dependent effective potential method for accurate free energy calculations of solids, Phys. Rev. B Condens. Matter Mater. Phys. 87 (2013), doi:10.1103/PhysRevB.87.104111.

[43] K. Momma, F. Izumi, VESTA 3 for three-dimensional visualization of crystal, volumetric and morphology data, J. Appl. Crystallogr. 44 (2011) 1272–1276, doi:10.1107/S0021889811038970.

[44] M. Yin, P. Nash, Enthalpies of formation of selected Pd_2YZ Heusler compounds, Intermetallics 58 (2015) 15–19, doi:10.1016/j.intermet.2014.10.019.

[45] R.I. Barabash, O.M. Barabash, D. Popov, G. Shen, C. Park, W. Yang, Multiscale twin hierarchy in NiMnGa shape memory alloys with Fe and Cu, Acta Mater. 87 (2015) 344–349, doi:10.1016/j.actamat.2015.01.010.

[46] T. Waitz, D. Spišák, J. Hafner, H.P. Karnthaler, Size-dependent martensitic transformation path causing atomic-scale twinning of nanocrystalline NiTi shape memory alloys, Europhys. Lett. 71 (2005) 98–103, doi:10.1209/epl/i2005-10061-y.